Diagnostic Indicators for Shipboard Systems Using Non-Intrusive Load Monitoring

LT Thomas DeNucci, USCG; Robert Cox; Steven B. Leeb; James Paris; CDR Timothy J. McCoy, USN; Christopher Laughman; CDR William C. Greene, USN

***Abstract*—Field studies have demonstrated that the non-intrusive load monitor (NILM) can effectively evaluate the state of many electromechanical systems by analyzing the electrical power that they draw. This paper discusses NILM applications in the marine environment. Machinery power data collected from *USCGC SENECA* (*WMEC-906*), a 270-foot U.S. Coast Guard cutter, indicates that the NILM can successfully diagnose the failure of flexible couplings and the presence of leaks in cycling systems. This paper discusses both of these shipboard problems, and it details the methodology used to develop the metrics that diagnose them.**

I. Nomenclature

λ_{ds}	Direct-axis stator flux
λ_{qs}	Quadrature-axis stator flux
λ_{dr}	Direct-axis rotor flux
λ_{qr}	Quadrature-axis rotor flux
r_s	Stator resistance
r_r	Rotor resistance
X_m	Magnetizing reactance
X_{ls}	Stator leakage reactance
X_{lr}	Rotor leakage reactance
i_{ds}	Direct-axis stator current
i_{qs}	Quadrature-axis stator current
i_{dr}	Direct-axis rotor current
i_{qr}	Quadrature-axis rotor current
v_{ds}	Direct-axis stator voltage
v_{qs}	Quadrature-axis stator voltage
v_{dr}	Direct-axis rotor voltage
v_{qr}	Quadrature-axis rotor voltage
p	Number of pole pairs
ω	Frame speed
ω_r	Rotor mechanical speed
ω_p	Pump mechanical speed
θ_r	Rotor mechanical angle
θ_p	Pump mechanical angle
D	Damping coefficient
K	Spring stiffness coefficient
J_m	Moment of inertia of rotor
J_p	Moment of inertia of pump
τ_e	Electromagnetic torque
τ_l	Load torque

This work was supported by a grant from the Office of Naval Research under the ONR Control Challenge Project. The Grainger Foundation provided essential additional support.

The authors are with the Laboratory for Electromagnetic and Electronic Systems, Massachusetts Institute of Technology, Room 10-069, 77 Massachusetts Avenue, Cambridge, MA 02139, USA.

II. Introduction

In recent years the U.S. Navy has come to rely heavily on electrical systems. As a result, modern naval vessels have developed a strong need for devices capable of monitoring numerous electrical loads. The ideal tool for this task would be a system that can automate the analysis of sensor data while minimizing the number of required sensors. The non-intrusive load monitor (NILM) is one device that is capable of performing both of these functions. The key utility of the NILM is that it can determine both the operating schedule and also the health of the major loads on an electrical service using only measurements of the input voltage and aggregate current [1], [2].

Previous work presented in both [3] and [4] has shown that the NILM provides data that can be used to study the behavior of shipboard mechanical systems. The aim of this paper is to extend the work presented in [3] in order to demonstrate that the NILM can monitor and trend the status of several critical loads or systems automatically. This paper focuses specifically on two engineering systems aboard the *USCGC SENECA* (*WMEC-906*). In the first system observed, a NILM was used to study and to diagnose the failure of a mechanical coupling that joins the *SENECA*'s Auxiliary Seawater (ASW) pump to its motor. In the other system studied, which is the *SENECA*'s vacuum-assisted waste disposal system, NILM data was used to create a model that can help determine the existence of leaks. This model can be used to explain the behavior of many cycling systems.

III. Coupling Failure Diagnostic

Numerous systems aboard modern naval vessels use couplings in order to link pumps and other mechanical systems to their driving motors. The failure of such couplings can have a drastic impact on mission capability. For instance, the ASW system on *SENECA* has two pumps that are both linked to motors via rubber couplings, and these couplings have shown a tendency to fail prematurely (i.e. after approximately 8-13 motor starts). Such a high failure rate is troublesome, as the ASW system provides cooling water to vital shipboard loads such as the ship's service diesel generators. Thus, coupling failure can cause machinery to overheat and sustain damage. This section details the specifics of the problem observed aboard the *SENECA*, and it presents a metric that the NILM can use to identify an impending problem.

0-7803-9259-0/05/$20.00 ©2005 IEEE.

A. *Preliminary Analysis of SENECA ASW Data*

In order to investigate the effects of coupling failure in the *SENECA*'s ASW system, a fresh, standard-issue USCG coupling was installed and the pumps were cycled on and off several times. During each start, a NILM was configured to monitor the power delivered to the pumps. An example of the real power drawn during an ASW pump start is shown in Figure 1 (See [1] and [2] for a discussion of how the NILM computes power waveforms such as the one shown in Figure 1).

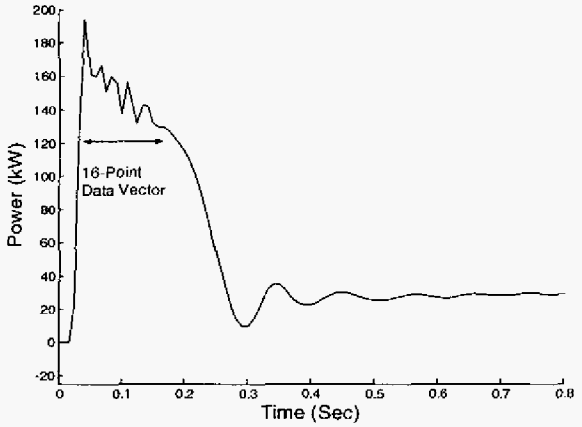

Fig. 1. Real power drawn during a typical ASW pump start. Note that the relative location of the 16-point data vector shown here was the same for each of the pump starts. The data shown here was sampled at 120Hz, which is the nominal sampling rate of the NILM.

Upon comparing the power drawn during each of the various pump starts, it was noticed that the amount of high frequency "ripple" present during the transient increased as the coupling progressively failed. In order to study this trend, we extracted a 16-point data vector from each waveform as shown in Figure 1 and computed its frequency spectrum using a 128-point, windowed discrete Fourier transform (DFT). Thus, we computed samples of the frequency spectrum [5] using the relation

$$X[k]=\sum_{n=0}^{127} x[n]w[n]e^{-j\frac{2\pi kn}{128}} \quad \text{for } 0 \le k \le 127, \quad (1)$$

where $x[n]$ is the zero-padded data vector, $w[n]$ is the zero-padded Hanning window, and $X[k]$ is the DFT of the sequence $x[n]w[n]$[1]. Figure 2 displays the magnitude of the resulting frequency spectrum for the 16-point data vector that is highlighted in Figure 1.

When analyzing the frequency content of the power drawn by the motor over successive starts, it was found that the amplitude of a spectral peak located at approximately 44Hz progressively increased as the coupling failed. This behavior can be seen in Figure 3. Figure 4 displays photographs of the coupling over a life cycle of use. To illustrate the physical origin of the observed amplitude change, we developed an induction motor simulation that would allow us try to reproduce the results shown in Figure 3 by varying specific motor parameters in a controlled fashion.

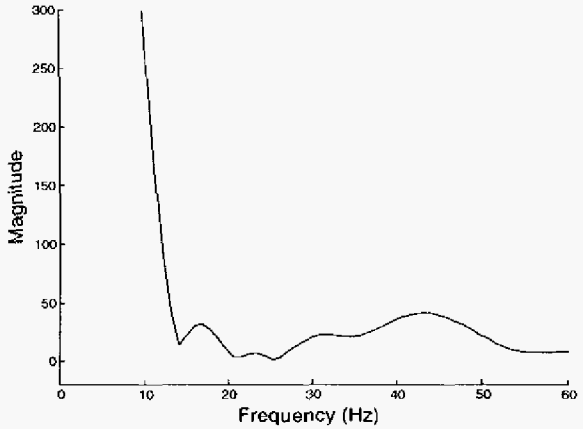

Fig. 2. Magnitude of the frequency spectrum of the windowed 16-point data vector shown in Figure 1.

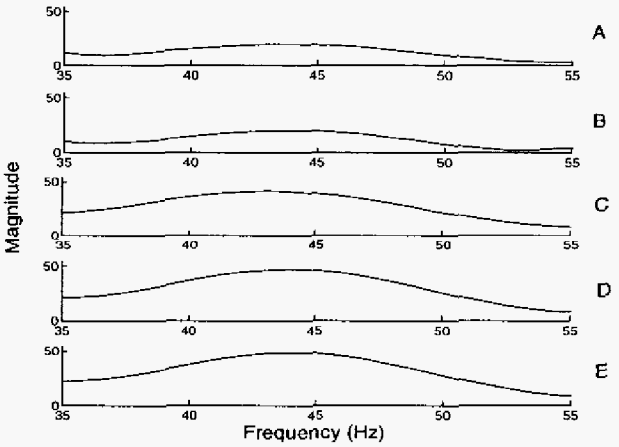

Fig. 3. Details of the high frequency segment of the magnitude of the frequency spectrum of P_f during several pump starts. The top trace was recorded after one of the first starts with a fresh coupling, and the bottom trace was recorded during the start before the coupling finally failed completely. Each start is designated by a letter written to the right of the corresponding trace.

B. *Induction Motor Simulation*

A critical requirement of the induction motor simulation developed to study the coupling failure aboard the *SENECA* was the inclusion of a model that could accurately describe the torsional dynamics of the mechanical system. This model, which has been employed by other researchers [6], describes an induction motor driving the inertia of a pump through a flexible coupling having a damping coefficient, D, and a spring stiffness factor, K (see Figure 5). For purposes of the simulation, the damper and the spring are assumed to have negligible moments of inertia.

[1] The DFT $X[k]$ contains N samples of the discrete-time Fourier transform of the windowed signal $x[n]w[n]$, which is denoted as $X(e^{j\omega})$. These samples are located at the radian frequencies $\omega_k = 2k\pi/128$. Thus, the samples also correspond to the continuous time frequencies $f_k = kf_s/128$, where f_s is the NILM's sampling rate [5].

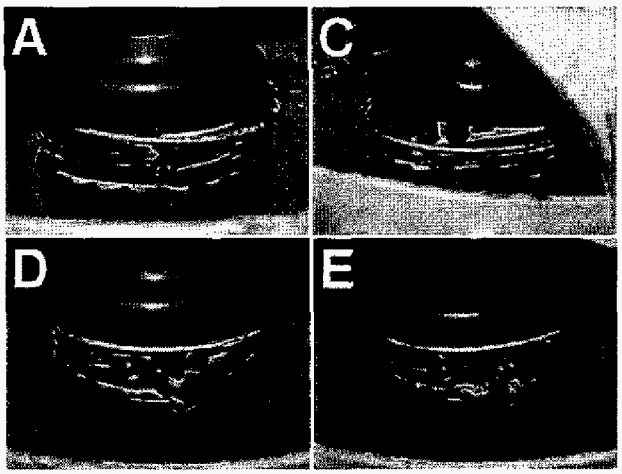

Fig. 4. Photographs showing the state of the coupling over a life cycle of use. The letters in each photograph correspond to the start letters displayed in Figure 3. Note the tearing that develops as the coupling deteriorates.

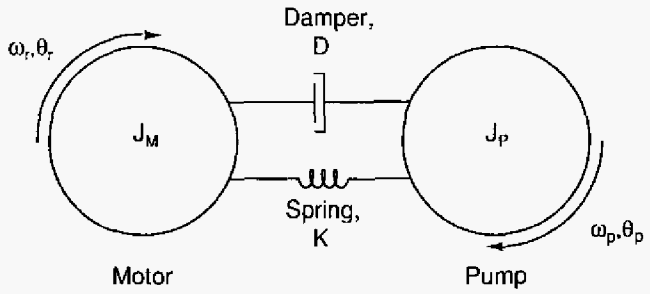

Fig. 5. Model for the mechanical subsystem. The pump and motor are considered to be separate inertias, and the coupling linking them is a combination of a damper and a spring. The mechanical speeds and displacements of both the pump and rotor are shown.

A set of state equations can be developed to describe the relationships between the various components of the mechanical model. These equations are based on the constitutive relations for rotational dampers and rotational springs. In terms of the variables presented in Figure 5, the torque applied to a rotational damper can be written in the form

$$\tau = D(\omega_r - \omega_p), \tag{2}$$

and the torque applied to a rotating spring can be written in the form

$$\tau = K(\theta_r - \theta_p). \tag{3}$$

Using these relations in combination with the electromagnetic torque, τ_e, the state equations for the mechanical model can be written as shown in (4)-(7).

$$\frac{\partial \omega_r}{\partial t} = \frac{D}{J_m}(\omega_p - \omega_r) + \frac{K}{J_m}(\theta_p - \theta_r) + \frac{\tau_e}{J_m} \tag{4}$$

$$\frac{\partial \theta_r}{\partial t} = \omega_r \tag{5}$$

$$\frac{\partial \omega_p}{\partial t} = \frac{D}{J_p}(\omega_r - \omega_p) + \frac{K}{J_p}(\theta_r - \theta_p) - \frac{\tau_l}{J_p} \tag{6}$$

$$\frac{\partial \theta_p}{\partial t} = \omega_p \tag{7}$$

In the simulation model, the load torque, τ_l, is of hydrodynamic origin. Assuming turbulent flow, that torque might be represented as $\beta\omega_p^2$, where β is a drag coefficient. It should be noted, however, that several different functional forms have been assumed for the load torque, and the results are qualitatively the same in each case [9].

A complete simulation model was created by combining the electrical state equations of the induction motor with the mechanical equations presented above. The electrical state equations in the synchronously rotating d-q reference frame [7] are given in (8)-(11).

$$\frac{\partial \lambda_{ds}}{\partial t} = v_{ds} + \omega\lambda_{qs} - r_s i_{ds} \tag{8}$$

$$\frac{\partial \lambda_{qs}}{\partial t} = v_{qs} - \omega\lambda_{ds} - r_s i_{qs} \tag{9}$$

$$\frac{\partial \lambda_{dr}}{\partial t} = v_{dr} + (\omega - p\omega_r)\lambda_{qr} - r_r i_{dr} \tag{10}$$

$$\frac{\partial \lambda_{qr}}{\partial t} = v_{qr} - (\omega - p\omega_r)\lambda_{dr} - r_r i_{qr}. \tag{11}$$

The overall 8^{th} order model was simulated in MATLAB. The parameters presented in [7] for a 50hp motor similar to that on-board the *SENECA* were used in the simulation. The simulation parameters are summarized in Table 1.

TABLE 1
INDUCTION MOTOR SIMULATION PARAMETERS

Parameter	Value
r_s	0.087 Ω
X_{ls}	0.302 Ω
X_m	13.08 Ω
X_{lr}	0.302 Ω
r_r	0.228 Ω
J_m	1.662 kg-m^2
J_p	0.95 kg-m^2
P	2
β	0.0045 N-m-s^2/rad^2

C. Simulation Results

In order to illustrate the effects of the spring and damper, several different simulations were conducted. In the first, the value of the damping coefficient was varied while the spring stiffness was held constant. Based on data from the coupling manufacturer [8], the spring stiffness was held at 150N-m/rad and the damping was swept from 0.5N-m-s/rad to 2N-m-s/rad in increments of 0.5N-m-s/rad. In each case, the NILM preprocessor computed the real power, P_l, using the simulated voltage and current. The frequency spectrum of the transient

power was then computed using (1).

Figure 6 shows the magnitude of the frequency spectrum for each of the different values of the damping coefficient. Note that just as in the case of the actual data, there is a high frequency spectral peak. In this case[2], that peak is centered at approximately 50Hz. Moreover, as shown in the inset plot in Figure 6, the amplitude of this spectral peak increases as the damping coefficient decreases. This result is in agreement with the experimental findings, as the damping coefficient is likely to decrease as the coupling deteriorates.

In order to observe the effects of the spring, a second simulation was performed in which the damping coefficient was held at 0.5N-m-s/rad and the spring stiffness was varied from 50N-m/rad to 200N-m/rad in increments of 50N-m/rad. The frequency spectra computed during these experiments appear in Figure 7.

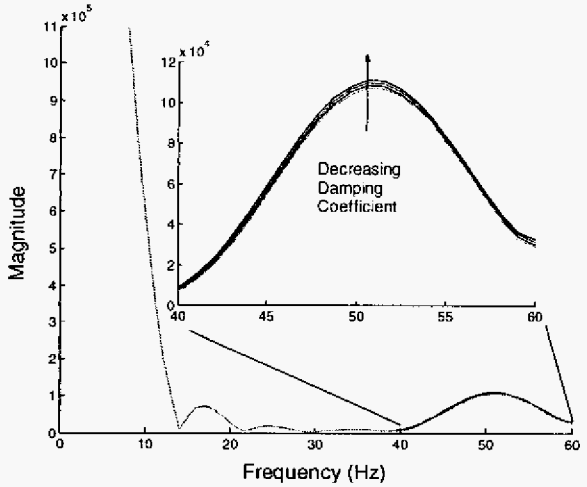

Fig. 6. Frequency spectrum of the transient section of P_1 as the damping coefficient varies. The inset plot shows the details in the area of the spectral peak located in the vicinity of 50Hz.

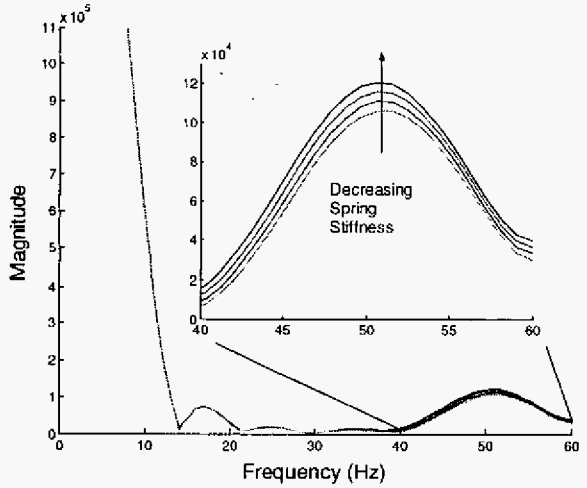

Fig. 7. Frequency spectrum of the transient section of P_1 as the spring stiffness coefficient varies. The inset plot shows the details in the area of the spectral peak located in the vicinity of 50Hz.

[2] It should be noted that the location of the high frequency peak observed in the simulation is not the same as in the experimental data. This is to expected since we are not using the actual ASW motor parameters in our simulation.

The results shown in Figure 7 are quite similar to those presented in Figure 6. As the coupling loses stiffness, the magnitude of the frequency spectrum in the vicinity of 50Hz again progressively increases. This behavior is also consistent with the experimental results, as a flexible coupling loses significant stiffness as it ages and tears.

A third set of simulations was conducted in which each value of the damping coefficient was used with each value of the stiffness factor. Figure 8 shows a plot of the peak value of the magnitude of the DFT for each combination of spring stiffness and damping coefficient.

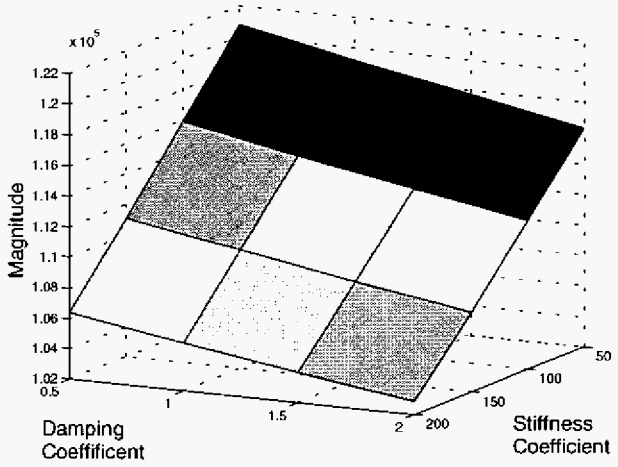

Fig. 8. Surface plot showing the value of the magnitude of the high frequency spectral peak for each combination of stiffness and damping coefficient that was considered.

D. Diagnostic Indicator

Both the experimental and simulated results presented here suggest that a way to diagnose deteriorating coupling conditions is to trend the behavior of the high frequency spectral peak observed in Figures 2 and 3. Our preliminary diagnostic software uses the three key steps listed below:

1.) DFT Computation: First, the DFT, $X[k]$, of a windowed, 16-point segment of the real power drawn during a motor start is computed using (1).

2.) Peak Frequency Location: Next, the DFT samples spanning the frequency band from 30Hz to 60Hz are searched to find the location of the largest spectral peak in that band. The location of this peak is denoted as ω_p in radian frequency (Note that this can be related to the corresponding continuous time frequency, f_p, via the relation $\omega_p = 2\pi(f_p / f_s)$).

3.) Diagnostic Indicator Computation: Finally, we compute the energy in a band of frequencies centered around ω_p. Assuming that this band spans from ω_p-$\Delta\omega$ to ω_p+$\Delta\omega$, the total energy it contains is given by [5]

$$E = \frac{1}{2\pi} \int_{\omega_p-\Delta\omega}^{\omega_p+\Delta\omega} \left| X(e^{j\omega}) \right|^2 d\omega \,, \qquad (12)$$

where $X(e^{j\omega})$ is the discrete-time Fourier transform (DTFT)

of the windowed sequence $x[n]w[n]$. Since the DFT $X[k]$ contains samples of $X(e^{j\omega})$ at the frequencies $\omega_k = (2\pi k)/128$, we calculate an estimate of the energy, E, using the DFT samples. The estimated value of E is the diagnostic indicator value.

Table 2 summarizes the diagnostic indicator values corresponding to each of the actual ASW pump starts used to form Figure 3. Note that this value significantly increases between starts B and C. If this sort of behavior were to be observed in the field, the NILM could immediately alert the Engineer Officer (EO). This would allow his staff to check the coupling well before a mission-critical failure.

TABLE 2
COUPLING DIAGNOSTIC INDICATOR VALUE FOR EACH OF THE STARTS USED TO FORM FIGURE 3

Start Letter (See Fig. 3)	Diagnostic Value
A	23.7
B	22.7
C	112.5
D	139.2
E	146.2

The indicator used here can reliably predict coupling failure in the *SENECA*'s ASW system. In practice, the NILM might provide indicator values to the EO in the form of a regular status report showing how the value has changed over the past several starts.

IV. SENECA SEWAGE SYSTEM DIAGNOSTIC INDICATOR

Modern naval vessels are equipped with numerous cycling systems that require periodic "charging" by an electromagnetic actuator such as a pump or compressor. Examples include compressed air systems and vacuum-assisted drains and disposals. It is common for systems of this variety to experience leaks that can force the controlling actuators to run too frequently. This problem has been observed several times in the sewage system aboard the *SENECA*. In that system wastewater is actively evacuated using a vacuum tank that is de-pressurized by two pumps. These pumps operate cyclically to maintain a desired pressure level.

Fortunately, a NILM can be used to determine the presence of a leak in cycling systems such as the *SENECA*'s sewage system. To perform this task, however, it is necessary for the NILM to be able to differentiate between periods of high usage and periods during which leaks exist. For this reason, experiments and simulations were conducted in order to study the behavior of the system under various conditions. This section describes in detail the problems observed in the *SENECA*'s sewage system, and it outlines a simple model that explains the observed behavior. This section concludes with a brief discussion of how the observed behavior can be used to develop a metric that can indicate the presence of a leak.

A. *Preliminary Analysis of SENECA Sewage System Behavior*

To study the operation of the *SENECA*'s sewage system, a NILM was installed and configured to record the time between pump runs[3]. The resulting observations were passed to software that creates a histogram showing the distribution of the time between pump runs over a given interval of time. Figure 9 shows the resulting histogram for a two-week period during which the *SENECA* was at sea. Numerous field tests have shown that this distribution is indicative of system behavior when there are no leaks present [9]. When leaks appear, however, the distribution markedly changes. For instance, Figure 10 shows the data recorded during a two-week period when the *SENECA*'s sewage system was using a faulty check valve [10]. In the presence of a leak, notice that there are significant changes in both the overall number of pump runs and in the amount of time elapsed between them.

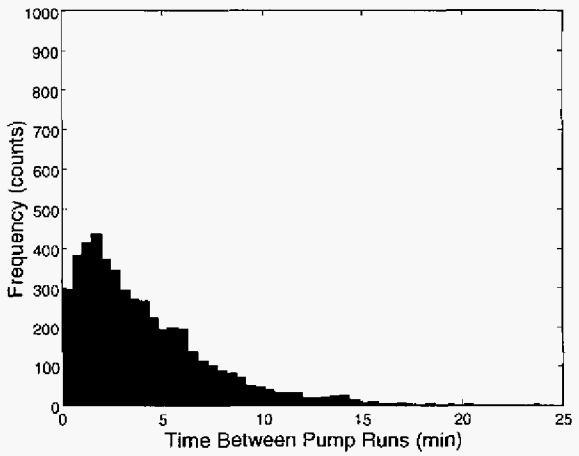

Fig. 9. Histogram showing the distribution of the time between pump runs over a two-week period during which no leaks were known to exist.

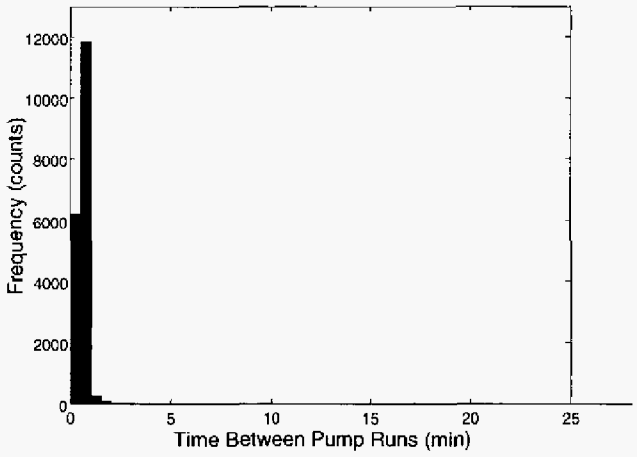

Fig. 10. Histogram showing the distribution of the time between pump runs over a two-week period during which the sewage system was known to have a faulty check valve.

[3] In this case, the time between pump runs is defined as the time elapsed between a pump shutdown and a subsequent pump start.

The experimental results presented in Figures 9 and 10 suggested that it would be wise to conduct a more controlled study of the *SENECA*'s sewage system. To begin this examination, several fixed leaks were inserted using a flow meter attached to the vacuum collection tank gauge line. In order to control the leak rate, the throttle valve on the flow meter was adjusted to achieve the desired flow rate. Data was collected for over 30 hours at each of 7 different leak rates while the ship was in port. Actual data recorded during each of the leak experiments is presented in Figure 11.

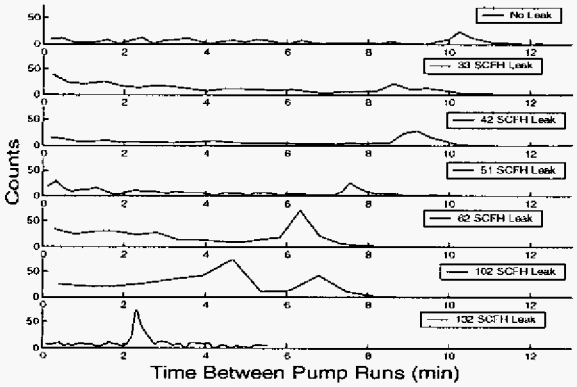

Fig 11. Histograms showing the distribution of the time between pump runs for several different leak rates. The leaks were introduced while the ship was in port. The peak observed in the no-leak case is likely due to background system loss.

The data displayed in Figure 11 demonstrates that the effect of a leak is to introduce a peak into the distribution of the time between pump runs. Noticeably, as the leak rate increases, the peak moves to the left, indicating that it forces the pumps to run more frequently. Additionally, an increased leak rate causes the new peak to increase in magnitude.

Although the trends observed in Figure 11 are consistent with the behavior seen in Figure 10, it is necessary to develop a complete model explaining both the observed baseline trends as well as the effects of leaks. Such a model is needed in order to develop a reasonable diagnostic indicator. Because it is difficult to control the human element in a system such as this, it is not possible to rely on experiments alone in order to create a model. For this reason, further study was conducted using a computer simulation.

B. MATLAB Simulation

Creating a simulation that accurately emulates the observed sewage system behavior required us to make several key assumptions about the system and its users. Most importantly, we needed to determine a model that describes the crew's flushing patterns, as these patterns control the baseline distribution for the time between pump runs. Using numerous experimental observations [9], it was found that the crew's flushing patterns are reasonably modeled using a Poisson process, which is one of several arrival-type stochastic processes that are commonly observed in nature [11].

When the arrival of events such as toilet flushes are governed by a Poisson process, the time between individual arrivals, T, is said to be a random variable that is distributed with an exponential PDF of the form

$$f_T(t) = \lambda e^{-\lambda t}, \tag{13}$$

where λ is a parameter known as the arrival rate of the process [11]. The choice of a Poisson model is shown to be qualitatively valid in the following presentation. A complete motivation for our model of the crew's flushing patterns is presented in [9].

In addition to choosing a model for the behavior of the crew, several other decisions had to be made before conducting a statistical simulation. Two critical assumptions used in our simulation are the following:

- Every flush instantaneously removes the same amount of vacuum from the sewage system.
- Leak rate is constant regardless of system pressure

In the actual simulation, the effects of flush events, leaks, and system charging by the vacuum pumps are all considered for a time interval equivalent to one week. The arrival of flush events required particular attention, as the time to the next flush is a random number selected from the exponential distribution in (13). The method used to choose this random value is described in detail in [9], [12], and[13].

C. Simulation Results

The simulation developed for this study was designed to model the situation in which both leaks and flushes occur simultaneously. In that general case, the current system pressure, P_r, is given by the relation

$$P_r = P_o - N\alpha_{flush} - t\alpha_{leak}, \tag{14}$$

where P_r is the current system pressure, P_o is the high pressure set point, N is a discrete-valued random variable representing the number of flushes that have occurred since the last pump run, t is the time since the last pump run, α_{flush} is the total amount of pressure removed by a single flush, and α_{leak} is the rate at which a leak bleeds pressure from the system.

In order to understand the simulation model, it is best to examine several limiting cases. First, consider the situation in which there is no leak present in the system so that only flushes can remove vacuum. In that event, (14) simplifies to

$$P_r = P_o - N\alpha_{flush}. \tag{15}$$

In order to determine the number of flushes, N_{max}, required to cause a pump run in the no leak case, (15) is solved to find the value of the variable N for which the overall system pressure falls below the low pressure set point. Thus, if the low-pressure set point is P_{low}, the value of N_{max} is

$$N_{\max} = \frac{P_o - P_{low}}{\alpha_{flush}}. \tag{16}$$

Equation (16) is an important result with two direct implications. First, it states that, in the absence of leaks, there is a fixed number of flushes that must always occur between subsequent pump runs. It also shows that the underlying distribution for the time between pump runs should be the

same as the distribution for the time to the arrival of the N_{max}-th flush. This result can be verified for any given set of sewage system parameters. For example, consider the simulated histogram shown in Figure 12, which was formed using the parameters outlined in Table 3. Also shown in Figure 12 is the least-squares fit of the data to the expected distribution of the time to the N_{max}-th flush. That distribution, which is equivalent to the PDF of the sum of the N_{max} inter-arrival times, is given by the formula [11]

$$f_Y(t) = f_{T_1}(t) * f_{T_2}(t) * \ldots * f_{T_{N_{max}}}(t)$$
$$= \frac{\lambda^{N_{max}} t^{N_{max}-1} e^{-\lambda t}}{(N_{max}-1)!}, \quad (17)$$

where Y is the sum of the inter-arrival times T_1 through T_{Nmax} and * is the convolution operator. Figure 12 shows that the simulated data fits quite well to the expected distribution. Additionally, note that the simulated results appear to be qualitatively the same as the baseline histogram shown in Figure 9.

TABLE 3
SIMULATION PARAMETERS IN THE NO-LEAK TEST CASE

Parameter	Value
P_{low}	14 in Hg
P_o	18 in Hg
α_{flush}	1 in Hg/flush
α_{leak}	0 in Hg/hour
λ	0.66 min^{-1}

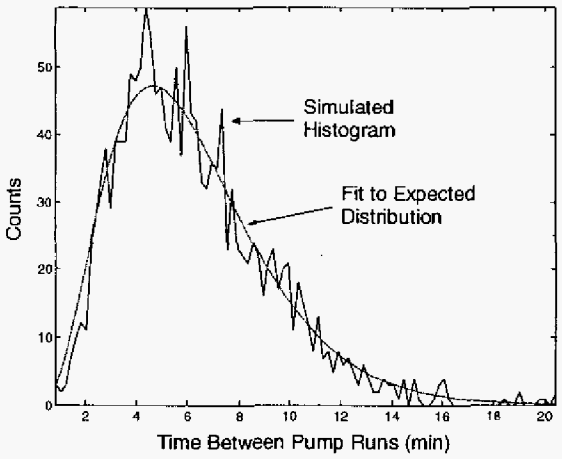

Fig. 12. The simulated histogram created using the parameters listed in Table 3 is shown. Superimposed on this histogram is the least-squares fit to the expected distribution presented in (17).

In the case in which the only source of pressure loss is a leak, (14) can be simplified to

$$P_r = P_o - t\alpha_{leak}, \quad (18)$$

which implies that the time increment between pump runs must be a fixed quantity. Additionally, it is true that the pressure lost between subsequent pump runs is a fixed quantity that is equivalent to the amount of pressure removed by the arrival of N_{max} flushes in the no-leak case. Thus, the time between pump runs in the leak-only case is denoted as t_{Nmax}.

In the general case in which both flushes and leaks remove pressure, the situation becomes more difficult to analyze. In this case it is necessary to determine how much time is required for the leak to decrease the pressure by an amount equal to one flush. That time, which is denoted as t_1, is defined to be the time at which the leak term, $t\alpha_{leak}$, is equal to the value of one flush drop, α_{flush}. Thus, the value of t_1 is given by the relation presented in (19).

$$t_1 = \frac{\alpha_{flush}}{\alpha_{leak}} \quad (19)$$

The time t_1 is extremely significant, as the behavior of the system drastically changes at that point. Prior to that time, the system behaves exactly the same as it does in the no-leak case. Thus, the only combination of events that can cause the pumps to cycle prior to t_1 is the arrival of N_{max} flushes. If, however, exactly $N_{\max} - 1$ flushes arrive before t_1, then the sum of the two loss terms at that time is equivalent to the pressure drop caused by N_{max} flushes. In that event, one of the pumps will run at time t_1. If fewer than $N_{\max} - 1$ flushes have arrived prior to t_1, however, the system will continue to wait on the arrival of new flushes.

Figure 13 displays the simulated histogram for a case with a small leak. For the simulation parameters listed in Table 4, (19) shows that t_1 is 12 minutes. Thus, on the basis of the previous argument, it is expected that a discontinuity should appear in the histogram at that time, and Figure 13 shows that to be true.

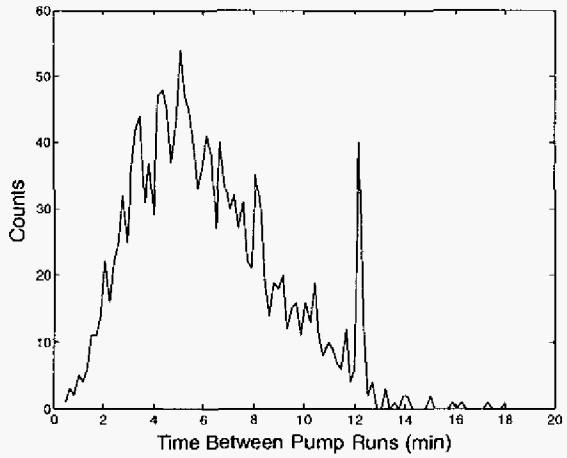

Fig. 13. Simulated histogram in the case in which the leak has a rate of 5inHg/hour. Note the sharp discontinuity at t_1=12min.

TABLE 4
SIMULATION PARAMETERS IN THE GENERAL TEST CASE

Parameter	Value
P_{low}	14 in Hg
P_o	18 in Hg
α_{flush}	1 in Hg/flush
α_{leak}	5 in Hg/hour
λ	0.66 min^{-1}

The argument explaining the system's behavior at t_1 can be extended to explain its behavior at the time $2t_1$, which is the point at which the leak has removed an amount of pressure equal to two flushes. At $2t_1$, one of the pumps will cycle if and only if exactly $N_{max}-2$ flushes have already arrived; otherwise, the system continues to wait. This argument can be generalized to explain system behavior at each integer multiple of t_1, up to the time $N_{max}t_1$. It should be noted, however, that not all discontinuities will necessarily appear in a given histogram, as it is possible that data must be collected for an extremely long period of time in order for all peaks to be observed.

Figure 14 shows a simulated histogram in which two peaks are observed. This histogram was formed using a 12inHg/hr leak rate and the baseline parameters listed in Table 4. For the given parameters, (19) shows that t_1 is 5min and that $2t_1$ is 10min. Discontinuities are observed at both of those times.

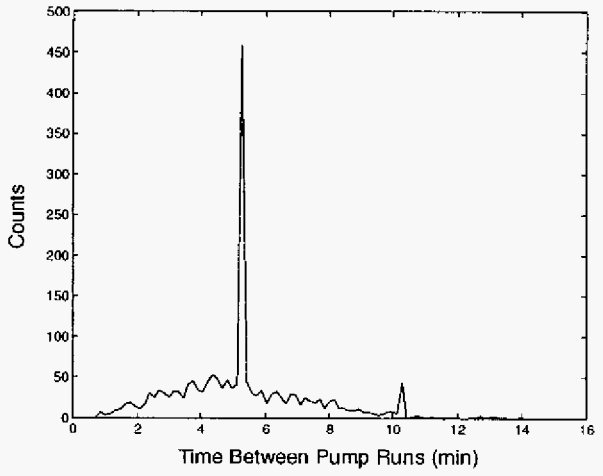

Fig. 14. Simulated histogram for a test case in which the leak has a rate of 12inHg/hr. Note that there are sharp discontinuities in the distribution at t_1=5min and $2t_1$=10min.

D. Diagnostic Indicator

There are a variety of ways in which the NILM can diagnose the existence of leaks in cycling systems. The most obvious method would be to present the Engineer Officer with a regular status report showing both the observed distribution over some fixed interval of time and the distribution that is typically observed over the same interval. The EO and his staff could then decide whether or not to investigate the system for the presence of a leak.

It is also possible that the NILM diagnostic software could perform more sophisticated analysis. For instance, the NILM could be pre-programmed to identify automatically all leaks with a rate greater than some minimum value. To find such leaks, the NILM would collect data for an interval of time long enough to be confident that the minimum detectable leak is discernable from random fluctuations in the background distribution. In that case, the NILM could apply a peak detection algorithm to the histogram of the observed data and alert the EO if any peaks exceed a minimum threshold.

Another possible diagnostic method would be to attempt to fit the histogram of the observed data to a model using a non-linear estimation procedure. Using this method, the NILM would attempt to fit recently observed data to an expected baseline distribution. The NILM could alert the EO in the event of a poor fit. Such a procedure could be used in concert with the other methods in order to further validate their findings.

V. Conclusion

This paper has shown that the NILM is capable of diagnosing problems in several critical shipboard engineering systems. In the first example, an indicator was developed to predict the failure of a mechanical coupling. This indicator was justified using models developed from sound physical theory. In the second example, indicators were proposed for diagnosing leaks in a cycling system. The use of these indicators was justified with a simulation that combines a physical model describing the behavior of the pumps with a statistical model describing the behavior of the humans who use the system. Thus, in both cases, physical modeling was used to validate the diagnostic indicators. The models developed here indicate that our diagnostic tools can be applied not only in the example systems, but also in systems exhibiting similar behavior.

References

[1] S. B. Leeb, J. L. Kirtley, and S.R. Shaw, "Transient Event Detection in Spectral Envelope Estimates for Non-Intrusive Load Monitoring," *IEEE Trans. on Power Delivery*, Vol. 10, pp. 1200-1210, 1995.

[2] L.K. Norford and S.B. Leeb, "Non-Intrusive Electrical Load Monitoring," *Energy and Buildings*, Vol. 24, pp. 51-64, 1996.

[3] J. S. Ramsey, et al., "Shipboard Applications of Non-Intrusive Load Monitoring," *ASNE Conference on Survivability and Reconfiguration*, Feb. 2005.

[4] W. C. Greene, et al., "Non-Intrusive Monitoring for Condition Based Maintenance," *ASNE Conference on Survivability and Reconfiguration*, Feb. 2005.

[5] A. V. Oppenheim and R.W. Schafer, *Discrete-Time Signal Processing*, Prentice-Hall, Upper Saddle River, NJ, 1999.

[6] A. A. Shaltout, "Analysis of Torsional Torques in Starting of Large Squirrel Cage Induction Motors," *IEEE Trans. on Energy Conversion*, Vol. 9, No. 1, pp. 135-142, March 1994.

[7] P. C. Krause, O. Wasynczuk, and S. Sudhoff, *Analysis of Electric Machinery*, McGraw-Hill, 1986.

[8] Sure-Flex Elasto-metric Couplings Product Guide, TB Wood's Incorporated, Chambersburg, PA.

[9] T. W. DeNucci, "Diagnostic Indicators for Shipboard Systems using Non-Intrusive Load Monitoring", SM Thesis, Department of Mechanical Engineering, MIT, Cambridge, MA, 2005.

[10] LT Michael Obar, personal communication, August 13, 2004.

[11] D. P. Bertsekas and J. N. Tsitsiklis, *Introduction to Probability*, Athena Scientific, Belmont, MA, 2002.

[12] Zwillinger, *CRC Standard Mathematical Tables and Formula*, CRC Press, New York, NY, 1996, pp. 595.

[13] P. R. Bevington, Data Reduction and Error Analysis for the Physical Sciences, McGraw-Hill, Boston, MA, 1992.